Journal of Magnetism and Magnetic Materials 422 (2017) 149–156

Contents lists available at ScienceDirect

Journal of Magnetism and Magnetic Materials

journal homepage: www.elsevier.com/locate/jmmm

The role of silicon on the microstructure and magnetic behaviour of nanostructured $(Fe_{0.7}Co_{0.3})_{100-x}Si_x$ powders

M. Hocine [a,g], A. Guittoum [b,*], M. Hemmous [b], D. Martínez-Blanco [c], P. Gorria [d], B. Rahal [b], J.A. Blanco [e], J.J. Sunol [f], A. Laggoun [g]

[a] Département de Génie Mécanique, Faculté de Technologies, Université de M'sila, B.P 166 Ichbelia, M'sila, Algeria
[b] Nuclear Research Centre of Algiers, 02Bd Frantz Fanon, BP 399, Alger-Gare, Algiers, Algeria
[c] SCTs, University of Oviedo, EPM, Mieres, 33600 Spain
[d] Department of Physics, EPI, University of Oviedo, Gijón, 33203 Spain
[e] Department of Physics, University of Oviedo, CalvoSotelo St., Oviedo, 330 07 Spain
[f] Departament de Fisica, Universitat de Girona, Campus de Montillivi, Girona, 17071 Spain
[g] UR-MPE, M'hamed Bougara University, Boumerdes, 35000 Algeria

ARTICLE INFO

Article history:
Received 12 October 2015
Received in revised form
24 July 2016
Accepted 20 August 2016
Available online 21 August 2016

Keywords:
FeCoSi compound
Nanostructured powders
Mechanical alloying
Structure
Magnetic properties

ABSTRACT

Single-phase$(Fe_{0.7}Co_{0.3})_{100-x}Si_x$ nanostructured powders (x=0,5, 10, 15 and 20) have been elaborated by mechanical alloying in order to investigate the effect of silicon on the microstructure and magnetic properties of these alloys. A disordered Fe(Co, Si) solid solution with body centred cubic (bcc) crystal structure is formed after 72 h of milling for all the compositions. The addition of Si gives rise to a progressive decrease of the lattice parameter, from about 2.865 Å for the binary $Fe_{70}Co_{30}$ compound down to 2.841 Å for the powder with x=20. The sample with the uppermost Si content exhibits the lowest value for the mean grain size (≈ 10 nm) as well as the largest microstrain (above 1.1%). All the samples are ferromagnetic at room temperature, although the saturation magnetization value reduces almost linearly by adding Si to the composition. A similar trend is observed for the hyperfine magnetic field obtained from the analysis of the room temperature Mössbauer spectra. The hyperfine field distributions show a broad double-peak shape for $x > 0$, which can be ascribed to multiple local environments for the Fe atoms inside a disordered solid solution.

1. Introduction

Many synthesis routes and processing methods are employed to elaborate nanostructured materials through chemical, physical and mechanical procedures [1]. Among these methods, the mechanical alloying (MA) technique is a solid-state powder processing technique that allows the fabrication of a huge variety of equilibrium and non-equilibrium alloys with either amorphous or nanocrystalline microstructure [2]. In particular, MA technique has been widely exploited to produce massive Fe-rich single-phase powder alloys aiming to determine the effect of microstructural changes in the magnetic behaviour [3–6]. During the MA process the elemental powders are repeatedly deformed, cold welded and fractured until achieving the equilibrium state at which the lowest grain size value is reached [2]. At this stage, and going down to the nanoscale level, it is well known that the microstructure is greatly modified and an important fraction of the atoms remain located at the grain boundaries. Then, the different local environments for the Fe atoms result in a modification of the magnetic behaviour compared with the conventional bulk alloys with the same composition [4,5,7,8].

Fe–Co alloys are known to be soft-magnetic materials due to the combination of high saturation magnetic polarization ($J_S \geq 2.45$ T) and permeability with low values for the magnetocrystalline anisotropy [9,10]. These features together with a high Curie temperature make these alloys very interesting for technological applications such as ultra high-density magnetic recording media, exchange-coupled nanocomposite magnets, or microwave devices [11,12]. Despite the fact that mechanically alloyed Fe-rich Fe–Co powders exhibit higher coercivity (H_C) due to introduction of internal strain during the alloying process [13,14], the correlation between microstructure and magnetic behaviour have been extensively investigated [5–7,15–20]. In particular, it has been reported that for 30 at% in Co the saturation magnetization (M_S) shows the maximum value along the whole compositional range [13,14].

On the other hand, the effect of a third element addition (Cu, V, Ni, Mo, Sn) on the mechanical and magnetic properties of the Fe–

* Corresponding author.
E-mail address: aguittoum@gmail.com (A. Guittoum).

http://dx.doi.org/10.1016/j.jmmm.2016.08.058
0304-8853/

Co system is currently being examined in detail [7,21–25]. A particular interest has been focused towards the Fe–Co-Si ternary system, where the formation of a bcc Fe(Co, Si) solid solution is observed [12,26] and a reduction of the magnetic anisotropy is found in $(Fe_{65}Co_{35})_{100-x}Si_x$ [12].

In this article we have selected the $Fe_{70}Co_{30}$ compound (the one with highest saturation magnetization) as the starting alloy, and we have explored what changes are induced on the microstructure by the progressive addition of Si (up to 20 at%). Besides, the variation of the room temperature magnetic properties and the hyperfine field distribution with the Si content is reported.

2. Experimental procedure

Elemental powders of Fe, Co and Si with purity of 99.99% (particle size $<100\ \mu m$) were mechanically alloyed to obtain single-phase $(Fe_{0.7}Co_{0.3})_{100-x}Si_x$ ($x=0$, 5, 10, 15 and 20) powders. The milling process was performed under argon atmosphere by means of a vario-planetary high-energy ball mill (Fritsch P4) working in a friction mode. Both the containers and balls (20 mm in diameter) are made of stainless steel. The ball-to-powder weight ratio was 15:1 for the five samples, with the same rotating speed (400 rpm) and a total milling time of 72 h that was selected in order to assure that single-phase alloys were formed. In order to prevent excessive temperature rise during the milling process a sequence of 30 min milling followed by 15 min pause was used.

The crystal structure and the values of the lattice parameters of the as-milled powders were determined from room temperature x-ray diffraction (XRD). The diffraction patterns were collected in a Philips X-Pert Pro powder diffractometer using Cu K_α radiation ($\lambda=1.5418$ Å) and a sealed Xe proportional detector. The measuring angular range, 2θ, was 10–120° with a step of 0.02° and counting times of 30 s per point in order to obtain good statistics. Additionally, the essential information about the microstructure, the values for the mean crystallite size, $<D>$ (nm), and for the lattice microstrain, $<\varepsilon>$ (%), were also estimated from the XRD patterns through the Williamson–Hall method [8,18,27–29]. This procedure is based on the line-broadening of the Bragg reflections and is given by the following equation:

$$\beta cos\theta = \frac{k\lambda}{D} + 2\varepsilon \sin\theta \quad (1)$$

where K is the Scherer constant, D the crystallite size, λ the wavelength of x-ray radiation, ε the lattice microstrain and θ is the Bragg angle. The parameter β is the full width at half-maximum of the Bragg peak (in fact, $\beta^2=\beta_{exp}{}^2-\beta_{inst}{}^2$, where β_{exp} is the measured width and β_{inst} is the instrumental width determined from the XRD pattern of a LaB_6 standard powder). The slope of the Williamson–Hall plot, $\beta\cos\theta$ vs.$2\sin\theta$, gives us the value of the lattice microstrain, ε, and the intercept with the $\beta\cos\theta$ axis gives the term $K\lambda/D$, and then the value for the mean crystallite size [26].

The chemical composition of the samples was checked with the energy-dispersive x-ray spectroscopy (EDS) option of the Philips XL 30 scanning electron microscope.

Differential scanning calorimetry (DSC) curves for all the samples were measured using a DSC Setsys equipment with argon as purging gas. The heating scans at a rate of 40 °C/min were recorded in the temperature range from 20 °C to 1200 °C. From the DSC curves the onset for temperature-induced strain relaxation and structural transformations, together with the values of the peak temperature and the enthalpy were determined for each sample.

The room temperature Mössbauer spectra were collected in transmission geometry with a constant-acceleration Wissel spectrometer, using a radioactive ^{57}Co source diffused into a Rhodium matrix. High-purity metallic iron (α-Fe) was used for energy calibration and also as a reference for the isomer shift. Mössbauer spectra were analyzed by means of the Recoil software using the Voigt-based hyperfine field distribution method (HFD-VB-F) [23]. We obtained the average hyperfine magnetic field $<H_{hf}>$ from the fit of the spectra, and its value is calculated through the following expression:

$$<H_{hf}>=\sum_i P_i(H_i)H_i \quad (2)$$

where H_i is the value of the magnetic field at the i^{th} site and $P_i(H_i)$ is the probability associated with the magnetic field H_i.

The magnetization vs. applied magnetic field curves, $M(H)$, were recorded at room temperature in a MicroSense Vibrating Sample Magnetometer (VSM), model EV9, within the applied magnetic field range of ± 22 kOe. Around 50 mg of mass were used for the measurements in order to minimize the noise in the magnetic signal. The values for the saturation magnetization and coercivity for the five powder samples were estimated from the $M(H)$ curves.

3. Results and discussion

3.1. XRD analysis

In Fig. 1a, the x-ray powder diffraction patterns for the five as-milled powders ($x=0$, 5, 10, 15, 20) are shown. In all the patterns only five peaks are observed, which can be associated with the Bragg reflections belonging to a body centred cubic (bcc) crystal structure with a lattice parameter close to that of α-Fe ($a=2.8664$ Å). There is not any evidence of additional peaks coming from a secondary phase, and/or oxide impurities. The refined value of the lattice parameter for the binary ($Fe_{70}Co_{30}$) alloy [$a=2.8651(3)$ Å] is slightly lower than that of α-Fe, and agrees with the values already reported for a disordered $Fe_{70}Co_{30}$ solid solution [11–13,17,26]. However, a shift of the Bragg peaks towards higher angles is observed as the silicon content is increased, thus indicating a progressive reduction of the unit cell due to smaller atomic radius of Si compared with those of Fe and Co. This fact is clearly evidenced in Fig. 1b, where the most intense peak associated with the (110) Bragg reflection is depicted. Fig. 2, displays that the evolution of the lattice parameter vs. Si content follows a non-linear behaviour. It is worth noting that the Bragg peaks do not show any shoulder, hence, we assume that the dissolution of both Co and Si atoms into the bcc-Fe lattice occupying substitutional positions is completed after 72 h of milling, giving rise to a single-phase ternary disordered solid solution.

There is another important feature that can be observed in Fig. 1a and b, a broadening of the Bragg peaks becomes evident as the Si content increases. The latter is a clear signature of important microstructural changes taking place during the milling processes, such as grain size reduction and the introduction of a considerable amount of lattice strain.

We show in Fig. 3 the evolution of the mean crystallite size, $<D>$, and the lattice microstrain, $<\varepsilon>$, as a function of silicon. The value of $<D>$ is around 40 nm for the as-milled binary alloy, and it drastically falls down to 20 nm for the alloy with $x=5$. The increment of Si above 5 at% provokes a further decrease of the mean crystallite size reaching a value of $<D>\approx 11(2)$ nm for $x=20$, but showing a less pronounced rate (see Fig. 3 and Table 1). We believe that the FeCoSi solid solutions become harder and stronger with more tendency to grain fragmentation as the amount of Si increases, leading to a diminution of the crystalline size [2,12,21]. In turns, $<\varepsilon>$ shows the opposite trend; the

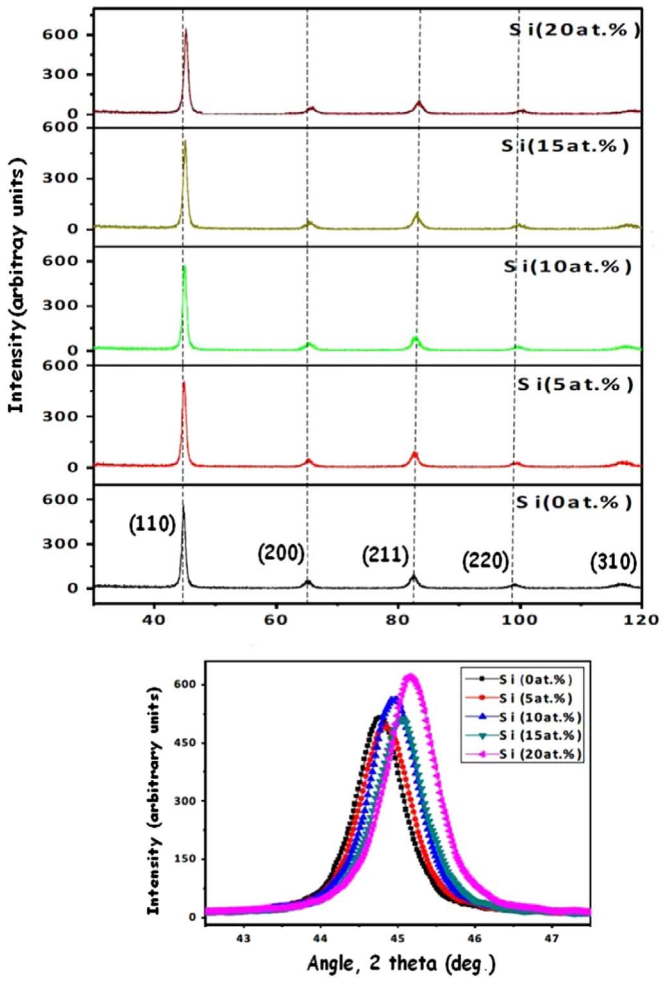

Fig. 1. (a) X-ray diffraction patterns for $(Fe_{0.7}Co_{0.3})_{100-x}Si_x$ powders. (b) Zoom of the most intense Bragg reflection (110).

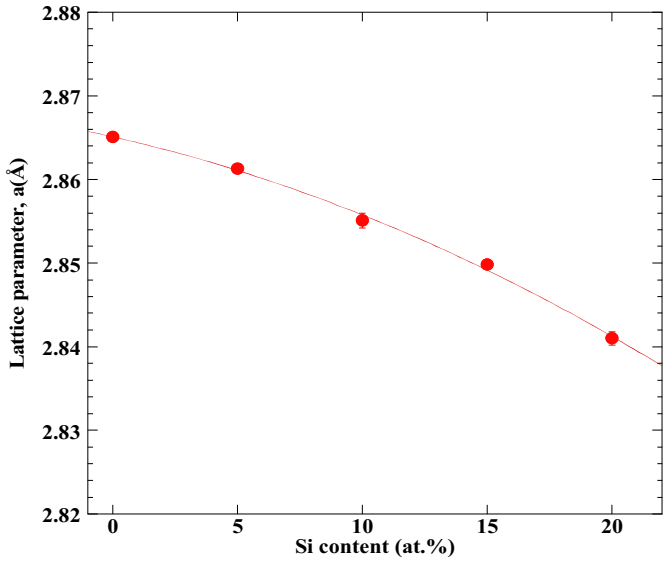

Fig. 2. Dependence of the lattice parameter with Si content in the $(Fe_{0.7}Co_{0.3})_{100-x}Si_x$ powders.

addition of silicon favours the introduction of lattice strain. Although the value of $<\varepsilon>$ is rather high in the binary $Fe_{70}Co_{30}$ alloy, above 0.7%, (similar to values found in other bcc-FeNi binary alloys [30]) it surpasses 1.1(1) % for the sample with higher

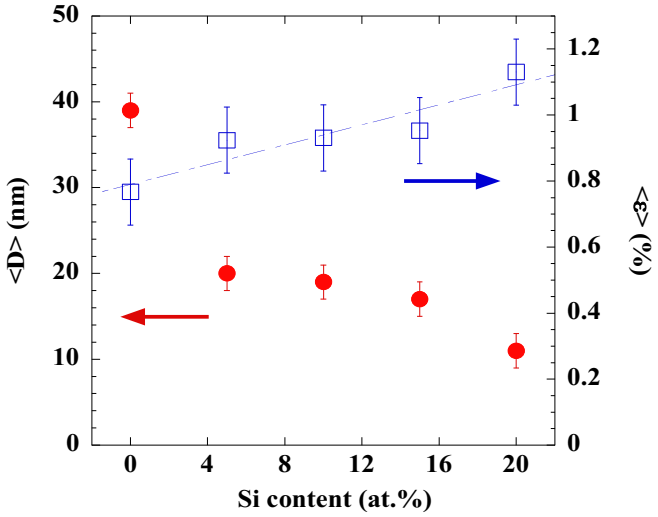

Fig. 3. Evolution of the average crystallite size (left y-axis) and microstrain (right y-axis) as a function of Si content.

Table 1
Values for the lattice parameter, a, mean crystalline size, $<D>$, lattice microstrain $<\varepsilon>$, saturation magnetization, M_S, hyperfine field corresponding with the maximum of H_{hf} distribution, H_{hf}^{peak}, and coercivity, H_C, for the $(Fe_{0.7}Co_{0.3})_{100-x}Si_x$ nanostructured powders.

Sample	$x=0$	$x=5$	$x=10$	$x=15$	$x=20$
a (Å)	2.8651(3)	2.8613(5)	2.8551(9)	2.8498(3)	2.8410(8)
$<D>$ (nm)	39(5)	20(3)	19(3)	17(2)	11(2)
$<\varepsilon>$ (%)	0.77(5)	0.92(7)	0.93(7)	0.95(8)	1.13(8)
M_S (emu/g)	223(5)	213(5)	199(5)	185(5)	162(5)
H_{hf}^{peak} (T)	36.1(2)	34.6(3)	33.2(3)	31.7(2)	29.6(2)
H_C (Oe)	42(4)	41(4)	42(4)	49(5)	52(5)

amount of Si ($x=20$). This fact could be attributed to an enhancement of the volume fraction occupied by the grain boundaries, which is a direct consequence of grain size reduction. During the milling process a large amount of mechanical energy is transferred to the powder system, giving rise to a disordering (creation of defects such as vacancies, stacking faults or dislocations) and grain boundary formation. At the nanometre length-scale the grain boundaries possess a more heterogeneous local structure compared with the nanocrystals (different average values for the nearest neighbour coordination and the atomic density, high density of defects, and therefore enhanced free volume), thus favouring the free energy storage in the system and the increase of the average microstrain [2]. In essence, this elastic energy stored at the grain boundaries enables the formation of supersaturated solid solution such as the $(Fe_{0.7}Co_{0.3})_{100-x}Si_x$ powders, with a total number of Co and Si solute atoms (44% for $x=20$) that is well beyond the solubility limit in bcc-Fe under equilibrium conditions. Therefore, if we take a look to Fig. 3 we could assume that there are two contributions to the observed values of microstrain. One of them originated during mechanical alloying process (severe deformation) that can reach 0.7%, being almost independent on the silicon content and that could be released by annealing. The second one comes from the alloying with silicon and scales almost linearly with the amount of Si (see Fig. 3).

3.2. Chemical composition

Energy dispersive X-ray analyses (EDS) were made on all the samples. In Fig. 4, we have presented EDS spectra for different milled samples. We have noted that only the peaks belonging to

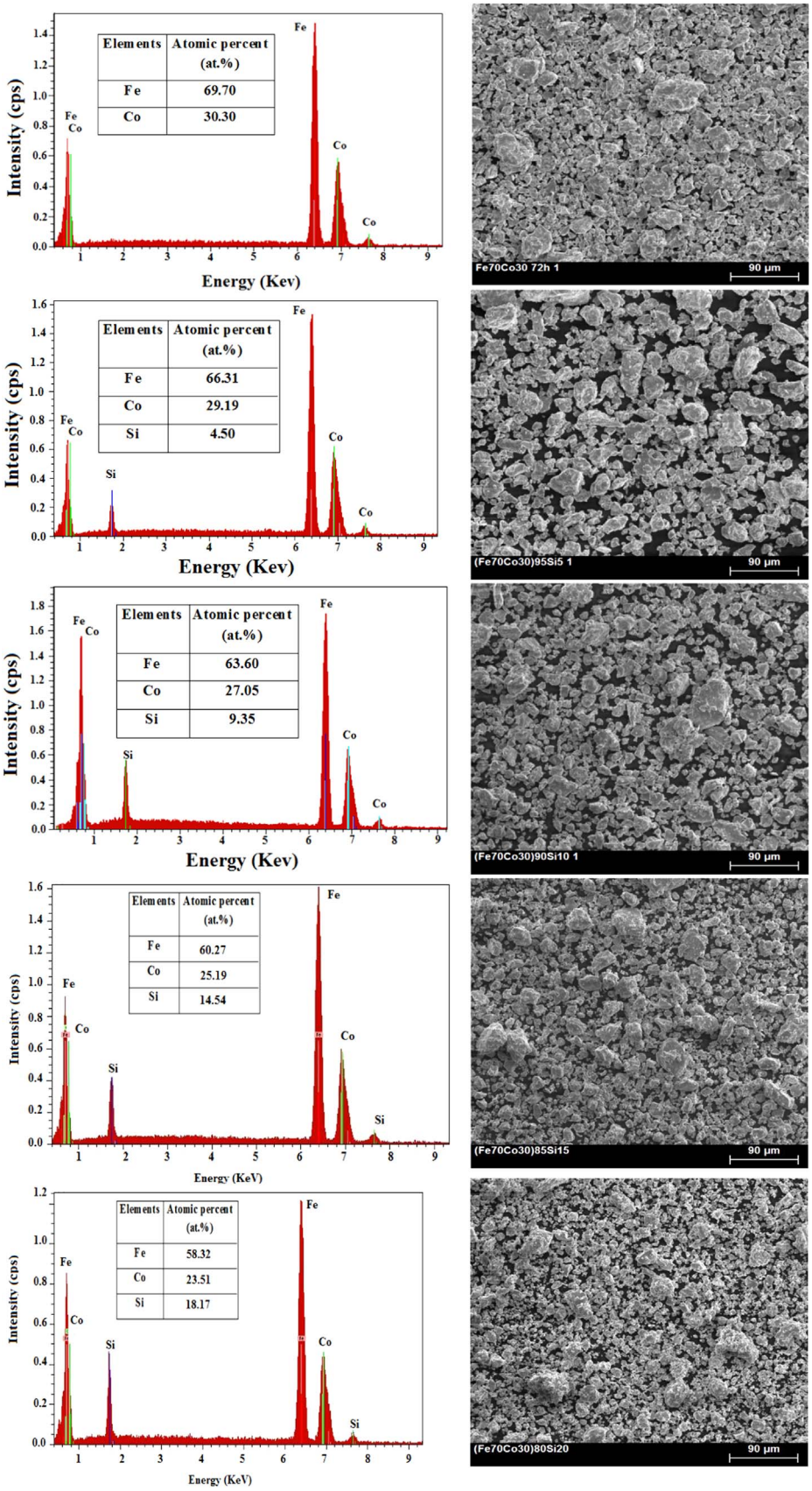

Fig. 4. EDS spectra with corresponding SEM micrographs for $(Fe_{0.7}Co_{0.3})_{100-x}Si_x$ samples (x=0, 5, 10, 15, 20).

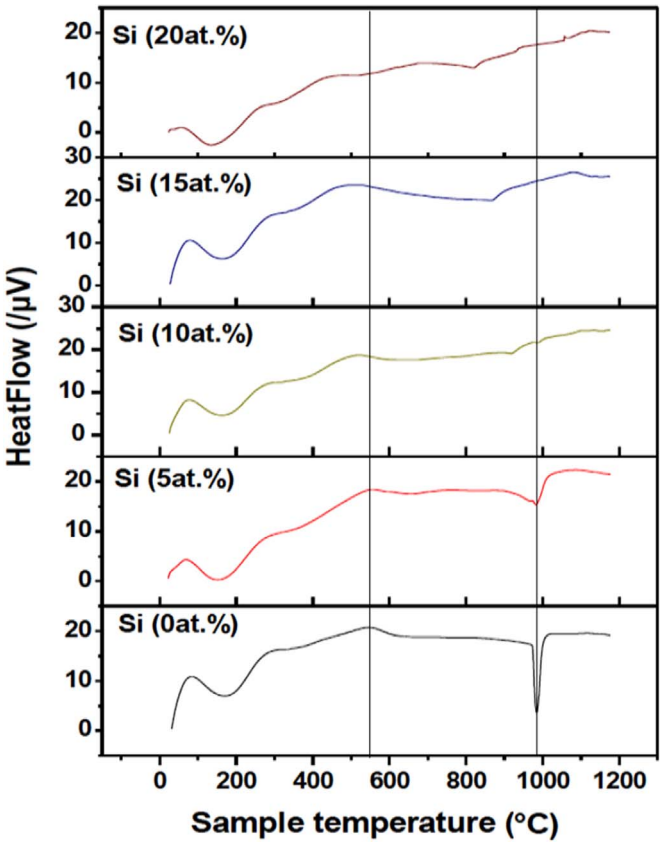

Fig. 5. DSC scans of $(Fe_{0.7}Co_{0.3})_{100-x}Si_x$ powders.

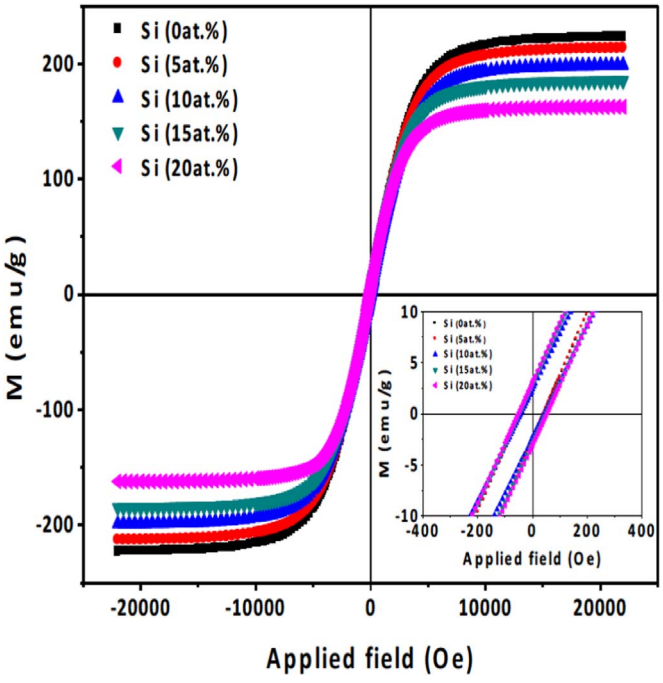

Fig. 6. Room temperature hysteresis loops for $(Fe_{0.7}Co_{0.3})_{100-x}Si_x$ samples.

Fe, Co and Si are present, hence, contamination from the vials and/or ball with other elements such as Cr, if present, is below 0.5%. For the quantification, we have performed standardless ZAF simulation of EDS spectra which confirmed that, for all samples, the composition is close to the starting powder.

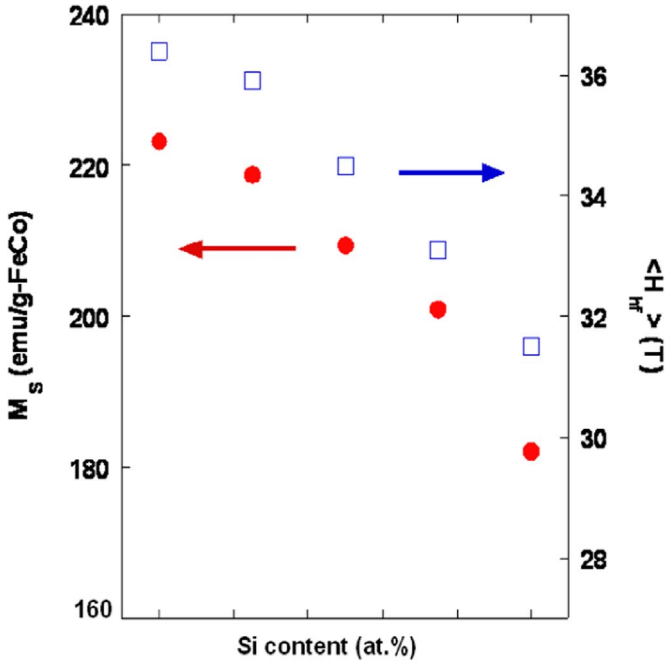

Fig. 7. Evolution of the normalized saturation magnetization (left) and maximum hyperfine field (right) with the Si content.

3.3. Differential Scanning Calorimetry

The thermal evolution of the as-milled $(Fe_{0.7}Co_{0.3})_{100-x}Si_x$ powders had been analyzed by means of differential scanning calorimetry (DSC). In Fig. 5, we show the DSC scans for all the samples measured data heating rate of 40 °C/min. On heating above 450 °C an exothermic peak indicates the onset of the structural transition from a disordered bcc to an ordered B2 (bcc) phase [31]. This peak is more evident for the binary alloy ($T \approx 550$ °C, in good agreement with that observed in conventional FeCo alloys [31]) and it is almost imperceptible for $x=20$. Moreover, the binary alloy exhibits a sharp high-temperature endothermic peak ($T \approx 984$ °C) corresponding with the α–γ (bcc to fcc) structural phase transition [31]. This α–γ phase transition also occurs for the $x=5$ sample at almost the same temperature (see Fig. 5), however, for higher Si content it seems that the presence of silicon stabilizes the bcc crystal structure at high temperature and inhibits the martensitic transformation.

The tiny endothermic peak above 800 °C for samples with $x=10$, 15 and 20 does not belong to any structural transformation, it is in fact the signature for the ferro-to-paramagnetic transition, which slightly diminishes on increasing the Si content, although it is still higher than that of α-Fe (770 °C). It is well known that the Curie temperature, T_C, for Fe-rich FeCo binary alloys climbs even above 900 °C with the addition of cobalt, up to around 25 at% of Co. For higher Co content the onset temperature for the structural phase transformation from α (bcc, ferromagnetic) to γ (fcc, paramagnetic) is below T_C of the alloy. The latter explains the absence of any tiny endothermic peak above 900 °C in the samples with $x=0$ and 5, because the expected value for T_C in these two alloys is larger than the temperature at which the α–γ phase transition takes place.

3.4. Magnetic behaviour

The room temperature magnetization vs. magnetic field curves, $M(H)$, for the five as-milled powders are depicted in Fig. 6. These curves exhibit the typical hysteresis loops of a ferromagnetic material. We have estimated the values for the saturation

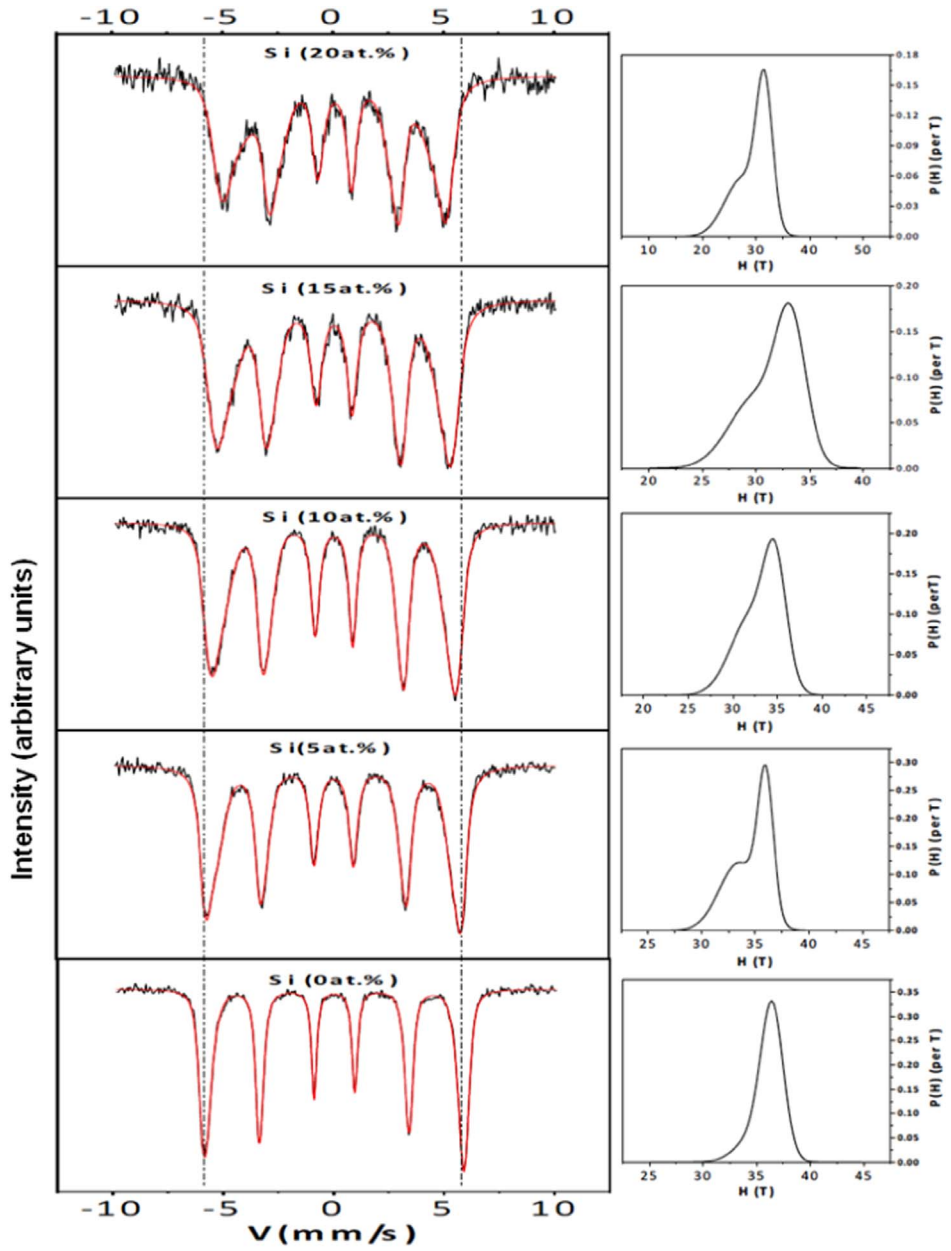

Fig. 8. Room temperature Mössbauer spectra and magnetic hyperfine field distributions for the five $(Fe_{0.7}Co_{0.3})_{100-x}Si_x$ as-milled powders.

magnetization, M_S, from the high magnetic field region of the M (H) curves using a fit to an approach-to-saturation law [32]:

$$M = M_S\left(1 - \frac{a}{H} - \frac{b}{H^2}\right) + \chi H \tag{3}$$

where a and b are coefficients related to defects (and/or micro-strain) and to crystal anisotropy, respectively, though χ is attributed to an independent field susceptibility. In our samples, the a/H term is very small and can be neglected [32]. The values for M_S and coercivity, H_C, are also included in Table 1. Although the value of the net saturation magnetization drops ca. 30% between the FeCo binary alloy and the powder with 20 at% in Si, if we calculate the normalized M_S value to the FeCo content, assuming that silicon does not carry any magnetic moment, this descent is not so large, (see Fig. 7, left y-axis). The reason for the diminution of the normalized saturation magnetization must be attributed to the electronic transfer from silicon atoms [32] that partially fill the 3d band of Fe and Co, thus giving rise to lower values for the magnetic moment of these atoms.

The value of coercivity remains almost constant up to $x=10$, and a slight enlargement is observed for the two alloys with higher Si content (see Table 1), which coincides with larger values for the microstrain. The measured values for H_C (about 40–50 Oe) are, in any way, similar to those found in other FeCoSi milled alloys [12,15].

3.5. Mössbauer analysis

The room temperature Mössbauer spectra and their corresponding hyperfine field distributions (HFD) for all the samples are shown in Fig. 8. The average values for the hyperfine magnetic fields, $< H_{hf} >$ were calculated from the HFD. It is clearly observed from the figure that the Mössbauer lines become more asymmetric and broaden progressively as silicon atoms are added, which is a clear signature of the increase of disorder in these bcc Fe–Co-Si ternary solid solutions [12,17,33]. The variations of the hyperfine

Table 2
Values for the average hyperfine magnetic fields for $(Fe_{0.8}Al_{0.2})_{100-x}Si_x$ alloys with the different possible atomic configurations in the first (NN) and in the second neighbour (NNN) shells around ^{57}Fe probe.

Si content (at%)	$\langle H \rangle_{hf}$ (T)	CS (mm/s)	(Fe, Co, Si) configurations		
			Configuration of NN shell	Configuration of NNN shell	Probability (%)
0	36.1082	0.03966	(6, 2, 0)	(4, 2, 0)	100
			(5, 3, 0)	(5, 1, 0)	80
			(7, 1, 0)	(3, 3, 0)	38
			(4, 4, 0)	(6, 0, 0)	17
5	34.5921	0.0517	(5, 3, 0)	(5, 0, 1)	100
			(4, 4, 0)	(5, 0, 1)	63
			(3, 5, 0)	(4, 0, 2)	31
			(7, 0, 1)	(1, 5, 0)	4
10	33.2481	0.0643	(5, 3, 0)	(4, 0, 2)	100
			(4, 4, 0)	(3, 0, 3)	58
			(6, 2, 0)	(5, 0, 1)	57
			(3, 5, 0)	(3, 0, 3)	27
			(7, 0, 1)	(2, 4, 0)	14
15	31.6984	0.0741	(5, 3, 0)	(3, 0, 3)	100
			(6, 2, 0)	(3, 0, 3)	75
			(4, 4, 0)	(2, 0, 4)	41
			(7, 1, 0)	(4, 0, 2)	36
			(7, 0, 1)	(4, 2, 0)	36
			(6, 0, 2)	(1, 5, 0)	10
20	29.632	0.0989	(6, 2, 0)	(2, 0, 4)	59
			(5, 3, 0)	(1, 0, 5)	29
			(7, 1, 0)	(2, 0, 4)	21
			(6, 0, 2)	(3, 3, 0)	100
			(6, 0, 2)	(4, 0, 2)	95
			(5, 0, 3)	(0, 6, 0)	4

parameters (average hyperfine magnetic field $< H_{hf} >$ and average isomer shift $< CS >$) with the addition of silicon can be shown in Table 2. The decrease in the value of $< H_{hf} >$ exhibits a similar trend to that of the normalized saturation magnetization (see Fig. 7 right y-axis), therefore, the origin for this behaviour can be also attributed to the electronic transfer from Si to the 3d shell of the Fe/Co atoms [34]. Moreover, the evolution of the average isomer shift with composition indicates that the shielding of the *s* electrons on the Fe nucleus is occurring for the alloys with higher Si content.

We have applied the local environment model to the fit of the spectra, in which the magnetic moment of an element depends on the number of nearest neighbours [35]. In Fe-X binary alloys, every atom X which substitutes an iron atom in the i^{th} coordination sphere of Fe causes the change of the hyperfine magnetic field at Fe site by the value of ΔH_i, the changes ΔH_i being additive. In practice, only the contributions from the first and the second coordination spheres are considered and the value H(m,n) of hyperfine magnetic field at Fe site may be described as [36]:

$$H(m, n) = H(0, 0) + m\,\Delta H_1 + n\,\Delta H_2 \quad (4)$$

where H (0,0) denotes the hyperfine magnetic field at Fe nucleus which is surrounded only by Fe atoms in the first and the second coordination spheres, m is the number of X atoms in the first sphere, n is the number of X atoms in the second sphere and ΔH_1, ΔH_2 the changes of the hyperfine magnetic field caused by X atoms in the first and second neighbour shells, respectively. For Fe–Si alloys, it is assumed that the hyperfine field at the Fe site decreases linearly with the number of Si atoms in the first and second neighbouring spheres [34]. For each Fe atom in the first shell substituted by Si, there is a reduction of $\Delta H_1 = 2.25$ T in the hyperfine field with respect to that of pure Fe; similarly, for each one of the second sphere results in a decrease of $\Delta H_2 = 1.17$ T. However, it is assumed that for Fe–Co alloys one Co atom increases the hyperfine field at Fe site by $\Delta H_1 = 0.8$ T and by $\Delta H_2 = 0.6$ T, in the first and second sphere respectively [37]. Using this model, the mean hyperfine field values have been attributed to the possible atomic configurations in the first (NN) and in the second neighbour (NNN) shells around the Fe atoms. The results are listed in Table 2.

For the binary compound $Fe_{70}Co_{30}$ ($x = 0\%$), the obtained value of $< H_{hf} > = 36.11$ T is in good agreement with that found by A. Zelenakova et al. $< H_{hf} > = 36.16$ T [19] using the same calulation method. This value of $< H_{hf} >$ corresponds to most probable configuration of (4Fe+4Co)] NN +[(4Fe+4Co) or 6Fe] NNN. With regards to the configuration results (see Table 2) the calculated probability for x=5 shows that no more than two atoms are present in the second coordination shell due to the low amount of Si in the sample, thus causing a small decrease in the values of $< H_{hf} >$. For $x = 10$, the configuration gives a high probability for the presence of one Si atom as first neighbour of the Fe atoms (see Table 2), in addition to the not negligible existence of more than two Si atoms in the second coordination shell. For $x > 10$, the probability of finding one or two Si atoms as NN increases as well as that corresponding to more than three Si atoms as NNN. The fact that Si atoms are present in the first coordination shell gives a clear explanation for the sharp decrease of $< H_{hf} >$ in these Fe–Co-Si solid solutions. Therefore, Mössbauer spectroscopy provides additional information about the existence of different magnetic environments for the Fe atoms and corroborates the results obtained for the magnetic measurements (see Section 3.4).

4. Summary and conclusions

We have studied the effect of silicon addition on the crystal structure, microstructure and magnetic properties of $(Fe_{0.7}Co_{0.3})_{100-x}Si_x$ ($x = 0$, 5, 10, 15 and 20 at%) powders prepared by mechanical alloying. The single-phase alloys were obtained after 72 h of milling time. We found that Si and Co atoms are

dissolved into the Fe lattice leading to the formation of a disordered bcc Fe(Co, Si) solid solution. The insertion of Si atoms into the $Fe_{70}Co_{30}$ binary system leads to a decrease in both the lattice parameter and the meancrystallite size reaching values around 10 nm for the $x=20$ powder. In contrast, the microstrain evolves towards higher values, being above 1% for the alloy with highest Si content. Mössbauer spectroscopy corroborates the formation of Fe (Co, Si) solid solution with different local environments for the Fe atoms. The average hyperfine magnetic field and the normalized saturation magnetization exhibit similar dependences as the amount of Si increases. Both magnitudes decrease as could be expected due to the electronic transfer from silicon that partially fills the 3d bands of Fe and Co atoms. These experimental findings could help in understanding the correlation between microstructure and magnetic behaviour in Fe-rich mechanically alloyed ternary alloys.

Acknowledgements

We thank SCT's of the University of Oviedo for the assistance in the XRD and magnetometry measurements. The authors from Spain acknowledge financial support from research projects MAT2014-56116-C4-2-R (Spanish MINECO) and FC-15-GRUPIN14-037 (Principality of Asturias Regional Government).

References

[1] C.C. Koch, Nanostructured Materials, Second ed., William Andrew, USA, 2007.
[2] C. Suryanarayana, Mechanical alloying and milling, Prog. Mater. Sci. 46 (2001) 1–184.
[3] P. Gorria, D. Martínez-Blanco, J.A. Blanco, A. Hernando, J.S. Garitaonandia, L. Fernández Barquín, J. Campo, R.I. Smith, Invar effect in FCC-FeCu solid solutions, Phys. Rev. B 69 (2004) 214421–214427.
[4] P. Gorria, D. Martínez-Blanco, M.J. Pérez, J.A. Blanco, Stress-induced large Curie temperature enhancement in $Fe_{64}Ni_{36}$ Invar alloy, Phys. Rev. B 80 (2009) 064421–064426.
[5] P. Álvarez, P. Gorria, V. Franco, J. Sánchez Marcos, M.J. Pérez, J.L. Sánchez Lamazares, I. Puente Orench, J.A. Blanco, Nanocrystalline Nd_2Fe_{17} synthesized byhigh-energy ball milling: crystal structure,microstructure and magnetic properties, J. Phys.: Condens. Matter, 22 (20109) 216005.
[6] N. Boukherroub, A. Guittoum, A. Laggoun, M. Hemmous, D. Martínez-Blanco, J. A. Blanco, N. Souami, P. Gorria, A. Bourzami, O. Lenoble, Microstructure and magnetic properties of nanostructured $(Fe_{0.8}Al_{0.2})_{100-x}Si_x$ alloy produced by mechanical alloying, J. Magn. Magn. Mater. 385 (2015) 151.
[7] A. Sharifati, S. Sharafi, Structure and magnetic properties of mechanically alloyed $(Fe_{70}Co_{30})_{91}Cu_9$ powder, Mater. Des. 36 (2012) 35–40.
[8] M.D. Chermahini, S. Sharafi, H. Shokrollahi, M. Zandrahimi, A. Shafyei, The evolution of heating rate on the microstructural and magnetic properties of milled nanostructured $Fe_{1-x}Co_x$($x=0.2$, 0.3, 0.4, 0.5 and 0.7) powders, J. Alloy. Compd. 484 (2009) 54–58.
[9] V. Mancier, J.L. Delplancke, J. Delwiche, M.J. Hubin-Franskin, C. Piquer, L. Rebbouh, F. Grandjean, Morphologic, magnetic, and Mossbauer spectral properties of $Fe_{75}Co_{25}$ nanoparticles prepared by ultrasound-assisted electrochemistry, J. Magn. Magn. Mater. 281 (2004) 27–35.
[10] J.G. Zhu, New heights for hard disk drives, Mater. Today 6 (2003) 22–23.
[11] N. Poudyal, C. Rong, Y. Zhang, D. Wang, M.J. Kramer, R.J. Hebert, J.P. Liu, Self-nanoscaling in FeCo alloys prepared via severe plastic deformation, J. Alloy. Compd. 521 (2012) 55–59.
[12] M. Yousefi, S. Sharafi, A. Mehrolhosseiny, Correlation between structural parameters and magnetic properties of ball milled nano-crystalline Fe–Co–Si powders, Adv. Powder Technol. 25 (2014) 752–760.
[13] Ch Kuhrt, L. Schultz, Formation and magnetic properties of nanocrystalline mechanically alloyed Fe–Co, J. Appl. Phys. 71 (1992) 1896.
[14] Ch Kuhrt, L. Schultz, Formation and magnetic properties of nanocrystalline mechanically alloyed Fe–Co and Fe–Ni, J. Appl. Phys. 73 (1993) 6588.
[15] A. Sharifati, S. Sharafi, Structural and magnetic properties of nanostructured $(Fe_{70}Co_{30})_{100-x}Cu_x$, alloy prepared by high energy ball milling, Mater. Des. 41 (2012) 8–15.
[16] Q. Zeng, I. Baker, V. McCreary, Z. Yan, Soft ferromagnetism in nanostructured mechanical alloying FeCo-based powders, J. Magn. Magn. Mater. 318 (2007) 28–38.
[17] M. Yousefi, S. Sharafi, The effect of simultaneous addition of Si and Co on microstructure and magnetic properties of nanostructured iron prepared by mechanical alloying, Mater. Des. 37 (2012) 325–333.
[18] B. Bhoi, V. Srinivas, V. Singh, Evolution of microstructure and magnetic properties of nanocrystalline $Fe_{70-x}Cu_xCo_{30}$ alloy prepared by mechanical alloying, J. Alloy. Compd. 496 (2010) 423–428.
[19] A. Zelenakova, D. Oleksakova, J. Degmova, J. Kovac, P. Kollar, M. Kusy, P. Sovak, Structural and magnetic properties of mechanically alloyed FeCo powders, J. Magn. Magn. Mater. 316 (2007) e519–e522.
[20] G. Herzer, Grain size dependence of coercivity and permeability in nanocrystalline ferromagnets, IEEE Trans. Magn. 26 (1990) 1397–1402.
[21] B. Chitsazan, H. Shokrollahi, A. Behvandi, O. Mirzaee, Characterization and magnetic coercivity of nanostructured $(Fe_{50}Co_{50})_{100-x}V_{x=0,2,4}$ powders containing a small amount of Co_3V intermetallic obtained by mechanical alloying, Powder Technol. 214 (2011) 105–110.
[22] D. Yuping, Z. Yahong, W. Tongmin, G. Shuchao, L. Xin, L. Xingjun, Evolution study of microstructure and electromagnetic behaviors of Fe–Co–Ni alloy with mechanical alloying, Mater. Sci. Eng. B 185 (2014) 86–93.
[23] H.A. Baghbaderani, S. Sharafi, M.D. Chermahini, Investigation of nanostructure formation mechanism and magnetic properties in $Fe_{45}Co_{45}Ni_{10}$ system synthesized by mechanical alloying, Powder Technol. 230 (2012) 241–246.
[24] H. Moumeni, A. Nemamcha, S. Alleg, J.M. Grenèche, Hyperfine interactions and structural features of Fe-44Co-6Mo (wt%) nanostructured powders, Mater. Chem. Phys. 138 (2013) 209–214.
[25] J.M. Loureiro, B.F.O. Costa, B. Malaman, G. Le Caër, S. Das, V.S. Amaral, Formation stages of bcc $(Fe_{44}Co_{44})Sn_{12}$ extended solid solution by mechanical alloying, J. Alloy. Compd. 25 (2014) 211–218.
[26] M. Khajepour, S. Sharafi, Characterization of nanostructured Fe–Co–Si powder alloy, Powder Technol. 232 (2012) 124–133.
[27] K. Akkouche, A. Guittoum, N. Boukherroub, N. Souami, Evolution of structure, microstructure and hyperfine properties of nanocrystalline $Fe_{50}Co_{50}$ powders prepared by mechanical alloying, J. Magn. Magn. Mater. 323 (2011) 2542–2548.
[28] J. Zhu, M. Mujahid, Development of nanocrystalline Fe–Co alloys using mechanical alloying, Mater. Sci. Technol. 21 (2005) 925–933.
[29] D. Martínez-Blanco, P. Gorria, J.A. Blanco, M.J. Pérez, J. Campo, Analaysis of the diffraction-line broadening on nanostructured Fe: size-strain effects induced by milling and heating, J. Phys.: Condens. Matter 20 (2008) 335213.
[30] D. Martínez-Blanco, P. Gorria, M.J. Pérez, J.A. Blanco, R.I. Smith, Martensite–austenite transformation in $Fe_{80}Ni_{20}$ ball-milled powder, J. Magn. Magn. Mater. 316 (2007) 328.
[31] T. Sourmail, Near equiatomic FeCo alloys: Constitution, mechanical and magnetic properties, Prog. Mater. Sci. 50 (2005) 816.
[32] B.D. Cullity, C.D. Graham, Introduction to Magnetic Materials, John Wiley & Sons, Inc, Hoboken, New Jersey, 2009.
[33] M. Khajepour, S. Sharafi, Structural and magnetic properties of nanostructured $Fe_{50}(Co_{50})-6.5$ wt% Si powder prepared by high energy ball milling, J. Alloy. Compd. 509 (2011) 7729–7737.
[34] M. Abdellaoui, C. Djega-Mariadassou, E. Gaffet, Structural study of Fe-Si nanostructured materials, J. Alloy. Comp. 256 (1997) 241 248.
[35] G.K. Wertheim, V. Jaccarino, J.H. Wernick, D.N.E. Buchanan, Range of the exchange interaction in iron alloys, Phys. Rev. Lett. 12 (1964) 24–27.
[36] E. Jartych, Local atomic order in nanocrystalline Fe-based alloys obtained by mechanical alloying, J. Magn. Magn. Mater. 265 (2003) 176–188.
[37] F.Z. Bentayeb, S. Alleg, B. Bouzabata, J.M. Grenèche, Study of alloying mechanisms of ball milled Fe–Cr and Fe–Cr–Co powders, J. Magn. Magn. Mater. 288 (2005) 282–296.